Size effect of resistivity due to surface roughness scattering in alternative interconnect metals: Cu, Co, Ru, and Mo

Chaoyu Hu,[1] Yu Zhang,[1] Zhiyi Chen,[1] Qingyun Zhang,[1] Jianjun Zhu,[2] Shaojian Hu,[2] and Youqi Ke[1,*]

[1]*School of Physical Science and Technology, ShanghaiTech University, Shanghai 201210, China*

[2]*Shanghai Integrated Circuit Reasearch and Development Center, Shanghai 201210, China*

(Received 13 February 2023; revised 28 April 2023; accepted 28 April 2023; published 12 May 2023)

The resistivity size effect of thin films due to atomically rough surfaces is investigated using first-principles quantum transport simulations with the disorder scattering treated by the nonequilibrium mean-field approach. Within the exact muffin-tin orbital–based first-principles method, the Madelung potential of film in device structure is constructed by implementing the boundary-condition correction. Cu(001), Co(0001), Ru(0001), and Mo(001) thin films are modeled with the thickness $d = 1$–10 nm. The random surface roughness is represented by an alloy model, consisting of one monolayer of M_xVa_{1-x} and $M_{1-x}Va_x$ on the respective top and bottom surfaces. The results of all metal films indicate that the first-principles resistivity ρ_s induced by surface roughness scattering is proportional to $1/d$. Our simulated resistivity results are consistent with the experimental measurements of epitaxial metal layers. We find that, for the same thickness, Mo films present the highest ρ_s, significantly larger than the other metals. The thin-film resisitivity ρ_s of Co is about 1.6 times that of Cu, while Ru results is slightly higher than Cu results. For all metal films, we obtain the parameter γ_s characterizing the intensity of surface roughness scattering as a function of x. Furthermore, we find the proportionality constant α_s versus x for the mean-free path $\lambda_s = \alpha_s \times d$ for surface roughness scattering. Our results show that at the high $x > 0.2$, α_s is rather close to a constant, with values of 4.5, 2.8, 2.1, and 1.0 for the respective Cu, Ru, Co, and Mo. We conclude that, compared to Co, Ru is competitive in resistivity size effect of surface roughness for an alternative to Cu interconnect for future technology nodes.

DOI: 10.1103/PhysRevB.107.195422

I. INTRODUCTION

Interconnects are the wires that connect billions of transistors in chips, transferring electrical signals, distributing clock signals, and providing power and ground. The interconnect resistance R, as described by

$$R = \rho \frac{L}{A}, \tag{1}$$

can be significantly increased by the downscaling of cross-section area A but is exacerbated by the size effect of resistivity ρ, especially for approaching the nanoscale. The electrical resistivity of Cu interconnects increases as their critical dimensions are comparable to or smaller than the electron mean free path, which is 40 nm for bulk Cu at room temperature [1–6]. For example, the resistivity is reported to be more than 3 times of bulk Cu when Cu interconnect line width approaches to 10 nm [6–8]. When the half pitch of interconnects reaches values of 10 nm and below, the increase of resistance presents challenges for the continuous downscaling of chips, aggravating resistance-capacitance delay, power consumption, and reliability risks [9]. The scientific and industrial community are therefore focused on mitigating the resistivity size effect and yielding highly conductive narrow interconnects to meet the conductance and reliability requirements.

In a physical picture, the resistivity is attributed to the momentum loss in the direction of the current when free electron scatters at lattice vibrations (phonons), impurities, defects, grain boundaries, and external surfaces. The resistivity size effect is primarily due to scattering at grain boundaries and scattering at external surfaces which is exacerbated by surface roughness. The convolution of these mechanisms [1,3,10,11] makes a quantitative study of electron scattering in metal interconnects challenging. Recent measurements on ultrathin epitaxial metal layers [12–17] indicated that the convoluted effect of scattering at grain boundaries was neglected and the surface scattering was reported to be the dominant contribution to the total resistivity and its size effect. The measured resistivity data of thin metal layers is usually described by the classical model of Fuchs-Sondheimer (FS) [18,19]. The FS model fits experimental data well for layer thickness close to or large than the electron mean free path but underestimates the measured resistivity for ultrathin (<20 nm) films [1,2,20–27]. In addition, the FS model predicts that resistivity of high-purity films will vanish at the zero-temperature limit. The intrinsic limitations of the FS model originates from its treatment of the surface with bulklike electronic structure. Later studies have proposed semiclassical [28,29] and quantum [30–33] models to describe the influence of surface roughness on thin-film resistivity without adjustable parameters. One basic assumption of these models is that surface scattering can be characterized by a mean free path λ_s that quantifies electron relaxation due to surface scattering [31,32]

*keyq@shanghaitech.edu.cn

instead of a partially specular boundary condition described by the specularity parameter p in the FS models. However, semiclassical and quantum models miss lots of specific aspects in the modeling of surface scattering in nanometric interconnects, for example, surface texture [34,35], surface micostructures [36], and surface chemistry [25,26,37,38], and the associated specific surface electronic states [38,39].

Recently, first-principles quantum transport simulations that account for atomic modeling have been applied to study surface scattering with full control over the determinant parameters, providing an accurate approach to model and understand the resistivity size effect. Several first-principles studies reported the resistivity change in Cu thin film due to various surface roughness and microstructure, including surface vibration modes [40], surface mounds [39], and surface discrete steps [41]. Other studies emphasized the influence of surface chemical bonding environment, reporting the resistivity change in Cu thin film during oxidation [37,42] or coated with metal layers [38]. The resistivity size effect induced by surface roughness was explored using the density functional theory (DFT) combined with nonequilibrium Green's function (NEGF) approach in the ultrathin Cu films with thickness $d \leqslant 2$ nm [43] and $d \leqslant 6$ nm [44]. Both studies suggested that the surface scattering brings about a resistivity that is proportional to $1/d$.

The major challenges for first-principles simulations of surface roughness have been associated with the treatment of disordered distribution on the surface. In the supercell-(SC) based first-principles methods, the disorder averaging is carried out by generating few random or quasirandom configurations in a finite supercell with periodic boundary condition, such as the simulations in Ref. [43]. However, the large computational cost greatly limits the applicability of the SC-based NEGF-DFT quantum transport method [40,43]. On the other hand, the nonequilibrium mean-field approaches employ the self-consistent construction of an effective medium to obtain disordered-averaged quantum transport properties, such as the coherent potential approximation plus nonequilibrium vertex correction [45,46] and nonequilibrium dynamical cluster approximation (NEDCA) [47,48]. The confinement of computational costs to the primitive cell level makes the nonequilibrium mean-field approach an attractive option for integration with first-principles quantum transport calculations to handle disorder scattering, suitable for the simulation of effects of disordered surface roughness scattering on electron transport.

For Cu interconnects, the barrier and liner layers with a certain thickness that are necessary for reliability further reduce the cross-section area available for Cu, aggravating the resistivity size effect and leading to a much stronger increase of the line resistance as dimensions shrink [5,7]. Therefore, the replacements of conventional metal Cu or W have been intensively researched, such ideal alternative metals should combine merits like low bulk resistivity, weak resistivity size effect, high resistance to electromigration and diffusion, and thus no need for barrier layers [17,49–52]. The Pt group metals [53], especially Ru [54,55], have been identified as promising candidates in fine dimensions, as well as Co [56,57], which has recently been introduced into industrial production [58,59]. Mo also shows competitivity with Cu metallization below the metal thickness of 8 nm [60].

In this study, we employ the exact muffin-tin orbital–(EMTO) based NEGF-DFT method in combination with the NEDCA to investigate the resistivity size effect of surface roughness in ultrathin films of alternative metals, including Ru, Co, Mo, and Cu. The thicknesses of the films is calculated up to 10 nm, which is consistent with experimental measurements and the interconnect half pitch in future technology nodes. We observe a strong agreement between our resistivity results and the $1/d$ dependence for a wide range of thickness $d \geqslant 1$ nm for all calculated metal films. We obtain the intensity parameter of surface roughness scattering γ_s, as well as the proportionality constant α_s in the mean free path $\lambda_s = \alpha_s \times d$ and their relation to roughness concentration to describe the surface roughness scattering in different metal films. Based on the present analysis of the resistivity size effect, we conclude that Ru is the optimal metal for replacing Cu in modern interconnect applications, compared to Co and Mo.

The rest of the paper is organized as follows. In Sec. II, we present the theoretical methods including the first-principles NEDCA-based quantum transport formalism within EMTO for the disordered device and the implementation of boundary condition correction of Madelung potential for the two-probe device structure; in Sec. III, we present the results and analysis; a short summary is included in Sec. IV.

II. METHOD

In this work, the conductance of thin films with varied lengths and thickness is computed by the EMTO-based first-principles quantum transport package, called SIGMAX, as developed in our previous representative works [47,61,62]. In SIGMAX, we have implemented both the scalar- and full-relativistic NEGF-DFT approach to compute quantum transport properties of the device from first principles [61,62] and combined with nonequilibrium dynamical cluster theory to effectively treat the effects of disorder scattering on the electron and spin transport through random defective structures [47]. In the following, we briefly introduce the EMTO-based first-principles quantum transport formalism and present the implementation of a general boundary-condition correction to the Madelung potential for a device structure with complex charge distribution in the semi-infinite electrodes to enable the simulations in this work.

A. EMTO-based quantum transport approach for disordered device

EMTO method utilizes the overlapped muffin-tin potential approximation to improve the accuracy and applies an important screening technique to realize a highly localized basis [63–68]. Within the EMTO method, the energy-dependent atom-centered basis is formulated as

$$\Phi^a_{RL}(\epsilon, \mathbf{r}_R) = \phi^a_{RL}(\epsilon, \mathbf{r}_R) - \varphi^a_{RL}(\epsilon, \mathbf{r}_R) + \psi^a_{RL}(\epsilon, \mathbf{r}_R), \quad (2)$$

where ϕ^a_{RL}, φ^a_{RL}, and ψ^a_{RL} denote the partial wave, free-electron solution, and screened spherical wave (SSW), respectively, while a represents the screening representation. For the sake

of completeness, we provide a brief overview of the EMTO (for a more comprehensive understanding of the EMTO formalism, we refer readers to Refs. [67,68]). The partial wave ϕ^a_{RL} is obtained by solving the local radial scalar-relativistic equation defined inside each overlapping potential sphere (s_R). The SSW ψ^a_{RL} satisfies the interstitial Schrödinger equation given by $[\nabla^2+\kappa^2]\psi^a_{RL}=0$, where $\kappa^2=\epsilon-v_{\rm mtz}$ denotes the kinetic energy, and the Muffin-tin zero $v_{\rm mtz}$ is a constant potential defined in the interstitial region. The SSW can generally be expanded around other sites R' as follows:

$$\psi^a_{RL}(\kappa^2,\mathbf{r}_R)=n^a_{RL}(\kappa^2,\mathbf{r}_R)\delta_{RR'}+\sum_{R'L'}j^a_{R'L'}(\kappa^2,\mathbf{r}_{R'})S^a_{R'L',RL}(\kappa^2), \tag{3}$$

where n^a_{RL} and j^a_{RL} represent the head and tail functions which are the linear combination of Neumann and Bessel functions, respectively, and S^a is the corresponding screened slope matrix. The SSW is derived by introducing a set of nonoverlapping screening spheres with radius a_{Rl} and then imposing boundary conditions such that it equals pure spherical harmonics on its own a_{Rl} sphere and vanishes on and inside the other $a_{R'l}$ spheres. In the region between the screening and potential spheres, the free electron solution φ^a_{Rl} is introduced, to ensure the EMTO's continuity at both a_R and s_R and differentiability at s_R,

$$\varphi^a_{Rl}(\epsilon,r_R)=n^a_{Rl}(\kappa^2,r_R)+j^a_{Rl}(\kappa^2,r_R)D^a_{Rl}(\epsilon), \tag{4}$$

Here $D^a_{Rl}(\epsilon)=D\{\varphi^a_{Rl}(\epsilon,a_R)\}$ represents the logarithmic derivative of the free-electron solution. By the above construction, EMTO exhibits continuity but are not differentiable, presenting kinks on the screening spheres. Within the EMTO method, the overlap and Hamiltonian matrices can be analytically derived to obtain

$$\langle\Phi^a|\Phi^a\rangle=a\dot{S}^a(\epsilon)-a\dot{D}^a(\epsilon), \tag{5}$$

$$\langle\Phi^a|\epsilon-\hat{H}|\Phi^a\rangle=aS^a(\epsilon)-aD^a(\epsilon), \tag{6}$$

where $\dot{D}^a$ and $\dot{S}^a$ denotes the energy derivative of D^a and S^a. As an important advantage, potential function D^a are the onsite quantity determined by the atom of each site, and S^a is the screened slope matrix only depending on the structure is a highly sparse matrix and thus provides the basis for the highly efficient calculation of Green's functions (GF).

To treat the quantum transport through the central device region between two semi-infinite electrodes as shown in Fig. 2(a), we utilize the contour-ordered GF in the Keldysh's 2×2 matrix representation [69], namely $\boldsymbol{G}=\begin{pmatrix}G^{\mathcal{A}} & 0\\ G^{\mathcal{K}} & G^{\mathcal{R}}\end{pmatrix}$ containing the retarded, advanced, and Keldysh's GFs, to account for the nonequilibrium quantum statistics. (Note that all the quantities in bold font in this section are contour-ordered quantities in the Keldysh's representation). Within the EMTO, Keldysh's NEGF for the central device region can be written as

$$\boldsymbol{G}_C=\left[a\boldsymbol{S}^a_C-a\boldsymbol{D}_C-\boldsymbol{\Sigma}_{ld,L}-\boldsymbol{\Sigma}_{ld,R}\right]^{-1}, \tag{7}$$

where the subscript C denotes the central region, and $\boldsymbol{S}^a_C=\begin{pmatrix}S^{a,\mathcal{A}}_C & 0\\ 0 & S^{a,\mathcal{R}}_C\end{pmatrix}$, $\boldsymbol{D}_C=\begin{pmatrix}D^{\mathcal{A}}_C & 0\\ 0 & D^{\mathcal{R}}_C\end{pmatrix}$, and $\boldsymbol{\Sigma}_{ld,L/R}=\begin{pmatrix}\Sigma^{\mathcal{A}}_{ld,L/R} & 0\\ \Sigma^{\mathcal{K}}_{ld,L/R} & \Sigma^{\mathcal{R}}_{ld,L/R}\end{pmatrix}$ for the self-energy due to left and right electrodes. For substitutionally disordered device regions, only the quantity $\boldsymbol{D}_C$ is random, featuring site-diagonal disorder. Therefore, the self-consistent mean-field algorithms, designed for the site-diagonal disorder, can be applied to compute the disorder averaged Keldysh's NEGF, namely $\overline{\boldsymbol{G}}_C$. In SIGMAX, we implemented the cluster-level mean-field theory, namely DCA, to construct an effective medium, described by the $\tilde{\boldsymbol{D}}^{\rm DCA}_C$, to obtain the average [47,48]

$$\overline{\boldsymbol{G}}_C=\left[a\boldsymbol{S}^a_C-a\tilde{\boldsymbol{D}}^{\rm DCA}_C-\boldsymbol{\Sigma}_{ld,L}-\boldsymbol{\Sigma}_{ld,R}\right]^{-1}. \tag{8}$$

$\tilde{\boldsymbol{D}}^{\rm DCA}_C$ features the full symmetry of the underlying lattice, providing high computational efficiency for the simulation of nonequilibrium disordered devices. For more technical details about the first-principles implementation of nonequilibrium DCA, please refer to Ref. [47]. After the DCA self-consistency for $\overline{\boldsymbol{G}}_C$, we can obtain all other real-time GFs as a linear combination of the GFs $\overline{G}^{\mathcal{R}/\mathcal{A}/\mathcal{K}}_C$, such as $\overline{G}^{<}_C=\frac{1}{2}(\overline{G}^{\mathcal{K}}_C+\overline{G}^{\mathcal{A}}_C-\overline{G}^{\mathcal{R}}_C)$. As an important result, the disorder averaged conductance is calculated as

$$\mathcal{G}=\frac{e^2}{h}\,\mathrm{Tr}\left[\overline{G^{\mathcal{R}}_C\Gamma_L G^{\mathcal{A}}_C\Gamma_R}\right]=\frac{e^2}{h}\,\mathrm{Tr}[-i\overline{G}^{<}_C\Gamma_R], \tag{9}$$

in which $\overline{G}^{<}_C$ contains the effects of multiple disorder scattering on the electron transport. Here $\Gamma_{L/R}\equiv i[\Sigma^{\mathcal{R}}_{ld,L/R}-\Sigma^{\mathcal{A}}_{ld,L/R}]$ are the linewidth function of left and right electrodes.

B. Boundary-condition correction to Madelung potential for device structures

In our simulation of the metal films in the two-probe structure, we employ the spherical cell approximation (SCA) proposed by Vitos [67,70] to construct the muffin-tin potential, namely

$$v_R(r_R)=v^I_R(r_R)+v^M_R(r_R), \tag{10}$$

where $v^I_R(r_R)$ and $v^M_R(r_R)$ are the potentials describing intracell and intercell interactions. The intercell contribution of the muffin-tin potential, usually called Madelung potential, describes the long-range electrostatic field generated by charges outside the potential sphere. In our two-probe device calculation, the contribution of semi-infinite electrodes with complex charge distribution is difficult to calculate by direct Ewald summation. We transform the electrostatics of the central region sandwiched by the two semi-infinite electrodes to an equivalent and general electrostatic system with a finite central region and well-defined boundary conditions. As a result, the Madelung potential of device $v^M_{\rm twop}$ can be written as

$$v^M_{\rm twop}(\vec{r})=v_c(\vec{r})+v_b(\vec{r}),$$
$$v_c(\vec{r})=\sum_{p=1}^{np}\sum_{pB,L}\varphi^{2d}_L(\vec{r}-p\vec{B})q_{pB,L}, \tag{11}$$

where $v_c(\vec{r})$ is the contribution of the multipole moments inside central region and $v_b(\vec{r})$ is the correction to satisfy the boundary condition that accounts for the influence of semi-infinite electrodes. Here $q_{p\vec{B},L}$ is the Lth multipole moment on

the site B in principal layer p and is calculated within SCA, and φ_L^{2d} is the potential produced by the unit Lth multipole moment of a layered structure and can be calculated with the Ewald technique [71]. For the disordered system, the disorder-averaged multipole moments have been calculated for each site.

The potential $v_b(\mathbf{r})$ fulfills the Poisson equation of a finite vacuum system with defined boundary conditions as follows:

$$\begin{aligned} \nabla^2 v_b(\vec{r}) &= 0, \\ v_b(\vec{r})|_{z=z_1} &= v^M_{\text{bulk,left}}(\vec{r}_\parallel, z_1) - v_c(\vec{r}_\parallel, z_1), \\ v_b(\vec{r})|_{z=z_2} &= v^M_{\text{bulk,right}}(\vec{r}_{||}, z_2) - v_c(\vec{r}_{||}, z_2), \end{aligned} \tag{12}$$

where the validity of the solution is assured by the uniqueness theorem, and the two boundaries are defined at the left and right extremities of the central region as $z = z_1$ and $z = z_2$ and the Dirichlet boundary conditions are set to the bulk results of electrodes. Here the bulk Madelung potential $v^M_{\text{bulk}}(\vec{r}) = \sum_{B,L} \varphi_L^{3d}(\vec{r} - \vec{B}) q_{B,L}$ can be calculated with the Ewald technique [71]. $v_b(\vec{r})$ preserves the translation invariance in each x-y plane along the z axis with translational vectors $\vec{a}_1$ and $\vec{a}_2$. To efficiently solve Eq. (12), we first uniformly discretize $v_b(\vec{r})$ in the x-y plane and then perform a two-dimensional (2D) DFT on the potential as follows:

$$\begin{aligned} v_b(\vec{r}_{\parallel,n}, z) &= \sum_m V_b(\vec{k}_{\parallel,m}, z) e^{i\vec{k}_{\parallel,m}\cdot\vec{r}_n}, \\ \vec{r}_{\parallel,n} &= \frac{n_1}{N_1}\vec{a}_1 + \frac{n_2}{N_2}\vec{a}_2, \\ \vec{k}_{\parallel,m} &= \frac{m_1}{N_1}\vec{b}_1 + \frac{m_2}{N_2}\vec{b}_2, \end{aligned} \tag{13}$$

in which $\vec{r}_{\parallel,n}$ and $\vec{k}_{\parallel,m}$ are the discrete points in the 2D cell spanned by lattice vectors $\vec{a}_1$ and $\vec{a}_2$ and in the Brillouin zone (BZ) spanned by the reciprocal lattice vectors $\vec{b}_1$ and $\vec{b}_2$. The indices $n = (n_1, n_2)$ is chosen such that $0 \leqslant n_1 \leqslant N_1 - 1$ and $0 \leqslant n_2 \leqslant N_2 - 1$, N_1 and N_2 is the number of points in $\vec{a}_1$ and $\vec{a}_2$ direction direction. $m = (m_1, m_2)$ is chosen as $-\frac{N_1}{2} \leqslant m_1 < \frac{N_1}{2}$ and $-\frac{N_2}{2} \leqslant m_2 < \frac{N_2}{2}$. $V_b(\vec{k}_{\parallel,m}, z)$ is the resulting potential in the reciprocal space. Equation (12) is efficiently solved in reciprocal space, and the solution for $V_b(\vec{k}_{\parallel,m}, z)$ can be found as

$$\begin{aligned} V_b(\vec{k}_{\parallel,m} \neq 0, z) &= A_m e^{|\vec{k}_{\parallel,m}|z} + B_m e^{-|\vec{k}_{\parallel,m}|z}, \\ V_b(\vec{k}_{\parallel,m} = 0, z) &= A_0 z + B_0, \end{aligned} \tag{14}$$

where the coefficients A_m and B_m are determined from the reciprocal boundary conditions, namely $V_b(\vec{k}_{\parallel,m}, z_1)$ and $V_b(\vec{k}_{\parallel,m}, z_2)$, which is calculated by applying the Fourier transform

$$V_b(\vec{k}_{\parallel,m}, z_{1/2}) = \frac{1}{N_1 N_2} \sum_n v_b(\vec{r}_{\parallel,n}, z_{1/2}) e^{-i\vec{k}_{\parallel,m}\cdot\vec{r}_{\parallel,n}}. \tag{15}$$

After obtaining $V_b(\vec{k}_{\parallel,m}, z)$ with the boundary condition, we can explicitly construct the Madelung potential of the two-probe device, namely

$$v_b(\vec{r}) = \sum_m V_b(\vec{k}_{\parallel,m}, z) e^{i\vec{k}_{\parallel,m}\cdot\vec{r}_\parallel}. \tag{16}$$

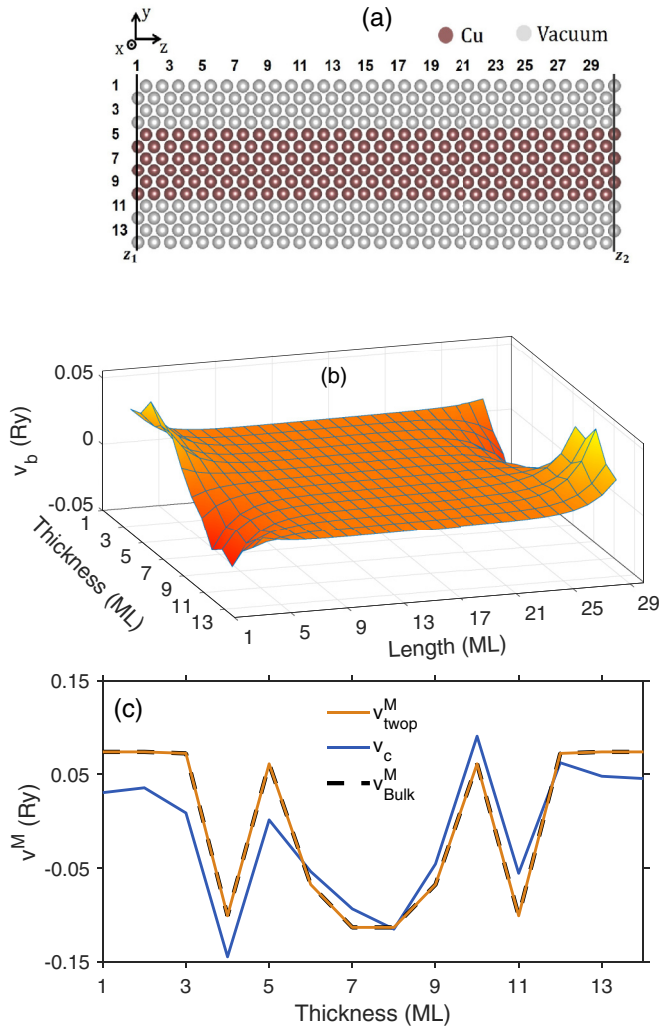

FIG. 1. (a) The front view of a six-ML-thick clean Cu film. Film thickness and length are oriented to the respective y and z axis. (b) The three-dimensional plot of the boundary-condition correction $v_b(r)$ in the y-z plane. (c) Comparison of $v_b(r)$ and $v_c(r)$ at boundary $z_{1/2}$ with the boundary value v^M_{bulk}.

It is noted that the accuracy of the boundary-condition correction to the Madelung potential described above is dependent on the size of the discrete grid.

As a test of our implementation of boundary-condition correction for the Madelung potential, we apply it to a clean Cu thin film containing six monolayers (ML) of Cu spheres and eight MLs of vacuum spheres (same radius as Cu) in thickness along the x axis as shown in Fig. 1(a). The perfect Cu film is modeled in a two-probe structure with the central device region 30-ML long along the z axis. For such a film, the results of the two-probe calculation should reproduce the Madelung potential in bulk calculations of Cu film. For simplicity, the v_b is presented in the y-z plane in Fig. 1(b). The profile of v_b is relatively flat and approaches zero near the center, showing that the v_c is already close to its bulk value. However, in the vicinity of the boundaries, v_b presents significant variation in magnitude, indicating the need for correction to the Madelung potential. As shown in Fig. 1(c), with the

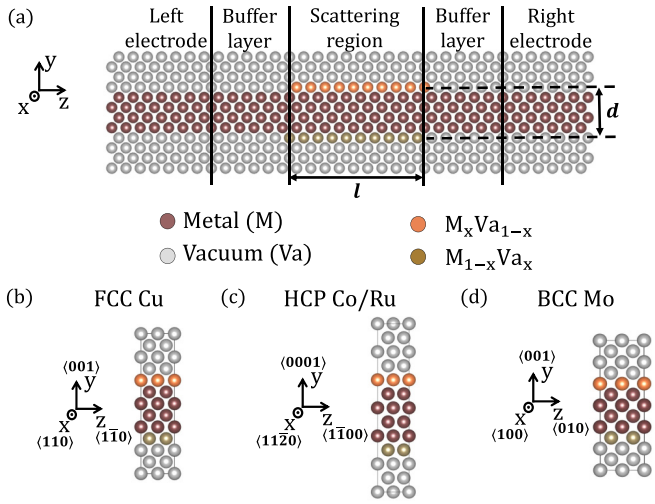

FIG. 2. (a) The front view of the metal thin film with thickness d. Film thickness and length are oriented to the y and z axis, respectively. Along the transport direction (z axis), the thin film is divided into two semi-infinite leads in the leftmost and rightmost, a scattering region with length l in the center and two buffers connecting the leads to the scattering region. Surface roughness is introduced in the scattering region by randomly adding metal adatoms with concentration x and $1-x$ at the top and bottom monolayers, respectively. The specific atomic structures of the scattering region are shown for FCC Cu thin film with (001) surface in (b), HCP Co and Ru thin film with (0001) surface in (c), and BCC Mo thin film with (001) surface in (d).

correction, the Madelung potential v^M_{twop} can exactly match the bulk value v^M_{bulk} (in dashed line) at the boundaries. The correct implementation of the boundary-condition correction to Madelung potential provides a foundation for simulating the quantum transport of metal films with roughness in two-probe structures.

III. RESULT AND DISSCUSION

The atomic modeling of the electron transport through the thin film is based on a two-probe device structure with the electrodes of perfect film, as shown in Fig. 2(a). The buffer layers have a fixed length of six MLs on each side of the left and right, which is long enough such that the bulklike conditions are matched at the boundaries in contact with the electrodes. The length l of the scattering region with disordered surface roughness is varied in our calculation to extract the resistivity. The two-probe thin-film device reserves periodic boundary conditions in the width (x) and thickness (y) directions. Six-ML vacuum spheres are used to separate neighboring films in the y direction. Surface roughness is introduced on the top and bottom surface of perfect crystal using a substitutional alloy model M_cVa_{1-c}, where metal adatoms (shown in yellow) randomly substitute for the vacuum sites. To maintain the thickness of the film unchanged with x, we consider the concentration $c = x$ and $c = 1-x$ at the respective top and bottom surface monolayers. To address the diagonal disorder problem in this random substitutional alloy model, we utilize the mean-field DCA method. Currently, the mean-field approach for modeling disorder cannot fully capture the impact of significant structural disorder, which leads to complex off-diagonal disorder and presents a long-term challenge for mean-field methods. (Although our recent efforts have made important progress for treating the off-diagonal disorder in mean-field framework, called auxiliary coherent medium theory [72–76], its combination with first-principles approach has not yet been realized.) As a result, our first-principles calculations are only constrained to simulate substitutional disorder without considering the geometry relaxation on surface adatoms. The thickness d of thin films is varied from 1 to 10 nm, and the number of atom sites in the central device region is varied from 100 to 2300. We consider four different metals, namely Cu (FCC), Co (HCP), Ru (HCP), and Mo (BCC) with the film unit cell as shown in Figs. 2(b), 2(c), and 2(d) (with five ML thick). We utilized the experimental lattice constants for each metal: $a = 3.615$ Å for Cu (FCC) [77]; $a = 2.507$ Å and $c = 4.070$ Å for Co (HCP) [78]; $a = 2.705$ Å and $c = 4.286$ Å for Ru (HCP) [79]; and for Mo (BCC) $a = 3.147$ Å [80]. It should be noted that HCP Co is in the ferromagnetic phase, leading to spin-polarized quantum transport in this system. We investigate the effect of surface roughness on the (001) surface in FCC Cu and (0001) surface in HCP Co and Ru, and (001) surface in BCC Mo.

All the calculations presented in this paper have been performed at zero temperature (in which we neglect the influence of finite-temperature-induced lattice distortion, namely the effects of frozen phonons.). The electronic structure is calculated with 20 energy points for complex energy contour, $60\times1\times30$ k-mesh for bulk 3D BZs, and 60×1 k-mesh for two probe 2D BZs. The conductance of thin films with varied lengths and thickness is computed based on the NEGF-DFT-DCA method as implemented in the package SIGMAX [47,61,62]. A local spin-density approximation exchange-correlation functional as parameterized in the Ref. [81] is employed in all our calculations. In the NEGF-DCA transport calculation, conductance is obtained at Fermi energy (E_F) with 120×1 k-mesh for 2D BZs, and the roughness disorder is treated with the single-site approximation in DCA (to well account for disorder scattering in the diffusive regime). Convergence tests are performed for all of these parameters to ensure the resistance results reported are converged.

We first present the resistance $R = \frac{1}{\mathcal{G}}$ of Cu, Co, Ru, and Mo thin film with 31 ML in thickness versus length l for different roughness concentration x as shown in Fig. 3. The 31-ML thickness corresponds to $d = 5.6$, 6.3, 6.6, and 4.9 nm in the respective Cu, Co, Ru, and Mo metal films. As shown in Fig. 3(a), for a fixed length l, the resistance shows a nonlinear dependence on surface roughness x: It increases most quickly at low concentration and reaches the maximal value at $x = 0.5$ in all metal films. For example, Cu film with $l = 2.04$ nm presents the resistance values of 0.735, 0.732, 0.726, 0.717, and 0.700 kΩ for the respective $x = 0.5, 0.4, 0.3, 0.2,$ and 0.1. It is found that the resistance of 31-ML-thick Mo thin film surpasses the results of other metals, despite its small cross-section area, while the resistance of 31-ML-thick Ru is the smallest compared to other metals. The results of Cu and Co films are close to each other. In particular, for $l = 3$ nm at $x = 0.5$, the R results of Cu, Co, Ru, and Mo thin films

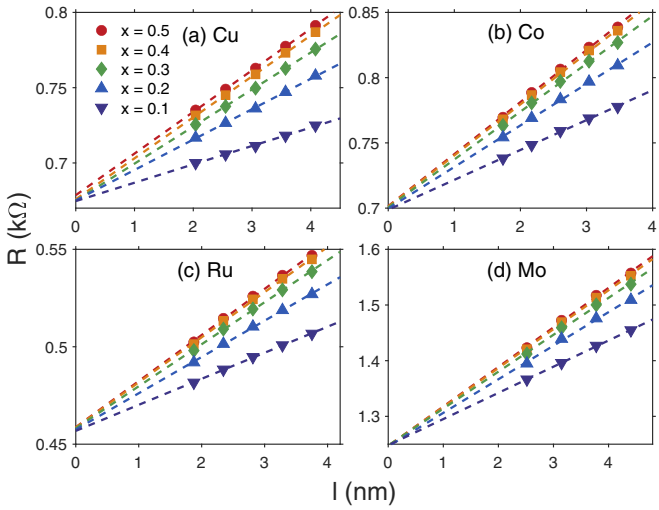

FIG. 3. Calculated resistance R vs scattering region length l for the thin film of Cu (a), Co (b), Ru (c), and Mo (d) with a thickness of 31 ML and roughness concentration of $x = 0.1, 0.2, 0.3, 0.4$, and 0.5. The dashed lines in the figure present the linear fitting of resistance R for length l.

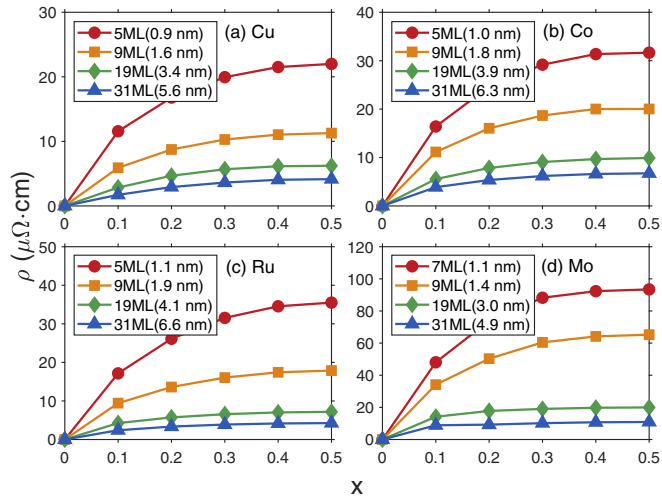

FIG. 4. Resistivity ρ_s vs roughness concentration x for different thicknesses d of Cu (a), Co (b), Ru (c), and Mo (d) thin films. Due to the symmetry of the system around $x = 0.5$, resistivity ρ_s induced by the two-sided roughness with concentration $x < 0.5$ are not shown.

present the values of 0.763, 0.823, 0.537, and 1.473 kΩ. Here the smallest value of resistance in Ru film suggests that Ru can be a promising alternative material for interconnects. Furthermore, the first-principles NEGF-DCA results show that the resistance R of all metal films increases linearly with increasing l. This behavior can be very well fitted by $R = R_0 + kl$, as shown by the dashed lines in Fig. 3 and shows the expected behavior of diffusive transport [82]. Here R_0 corresponds to the ballistic conductance of thin films, which takes into account the interface effect of the buffer layer and scattering region. It is observed that, for different x, the fitted dashed lines share almost the same R_0 at $l = 0$ as expected for ballistic transport. The Ru film presents the smallest R_0 value of 0.46 kΩ, while the respective R_0 values for the respective Cu, Co, and Mo films are 0.67, 0.70, and 1.25 kΩ. Once the slope k has been obtained by fitting first-principles results of R, the resistivity of different metal films with thickness d can be determined using $\rho_s = kwd$ (where w and d represent the width and thickness of the film, respectively).

The fitting process in Fig. 3 is repeated for different thicknesses and surface roughness to obtain the film resistivity dependence on the d and x for Cu, Co, Ru, and Mo. Resistivity results are shown in Fig. 4 as a function of roughness concentration x for different thicknesses d. The resistivity of thin films is symmetric around $x = 0.5$ because the roughness concentration of the top and the bottom surface is given by x and $1 - x$, respectively. As shown in Fig. 4, it is noted that the resistivity results for different thicknesses all reach the maximal at $x = 0.5$, which corresponds to the highest degree of roughness and the most diffusive scattering. At $x = 0$, the surface roughness scattering vanishes, presenting $\rho_s = 0$ for all metal films due to the specular scattering of perfect surfaces. In Fig. 4, the trend of ρ_s versus x is quite similar for different metal thin films: All curves present the fast increase at small x (below 0.2) while the increase for $x > 0.2$ is rather limited, presenting the important nonlinear dependence of ρ_s on the surface roughness. For instance, the resistivity of a five-ML-thick Cu thin film can be rapidly increased from zero for a perfect surface to 11.57 μΩ cm at $x = 0.1$ and 16.79 μΩ cm at $x = 0.2$. However, for higher x such as 0.3, 0.4, and 0.5, the increase in ρ_s is limited, and the values reach only 19.94, 21.52, and 22.00 μΩ cm, respectively. It is observed in Fig. 4(d) that the Mo film exhibits a significantly higher resistivity compared to the other films, while the Cu film in Fig. 4(a) has the lowest ρ_s values. For example, at $x = 0.2$ and $d \approx 1$ nm thick, the ρ_s values are 16.79, 24.66, 26.12, and 73.88 μΩ cm for the respective Cu, Ru, Co, and Mo. The resistivity results of Co and Ru film in Figs. 4(b) and 4(c) are close and acceptably higher than Cu, indicating that Ru and Co are promising candidates for interconnect metal. However, the significantly higher resistivity of Mo film makes it less appealing option for alternative interconnect metal. Moreover, as shown in Fig. 4, the resistivity of all metal films presents a significant dependence on thickness, with an increase in d resulting in a rapid decrease in ρ_s. In particular, in Fig. 4(c), at $x = 0.5$, the resistivity of the Ru thin film decreases rapidly from 35.50 μΩ cm for $d = 1.1$ nm to 17.88, 7.17, and 4.25 μΩ cm for $d = 1.9$, 4.1, and 6.6 nm, respectively, indicating the substantial size effect in ρ_s. The contribution of surface roughness scattering to film resistivity presents a $1/d$ dependence on thickness. To fit our resistivity data, we employ an expression as described by the following equation:

$$\rho_s = \frac{3}{8}\frac{\rho_0\lambda_0}{d}\gamma_s, \tag{17}$$

where ρ_0 and λ_0 are bulk resistivity and electron at room temperature, and d is the film thickness. The empirical parameter γ_s characterizes the intensity of surface scattering in the thin film and can be compared to $1 - p$, where p is the specularity parameter in the FS model. For the product of bulk resistivity and mean free path $\rho_0\lambda_0$, here we introduce the direct relation

TABLE I. List of interconnect metals Cu, Co, Ru, and Mo, sorted with increasing surface scattering intensity γ_0. The bulk room-temperature resistivity ρ_0 are from Ref. [51].

Element	R_BA (10^{-15} Ω m^2)	γ_0	σ (nm^{-1})	α_0	ρ_0 ($\mu\Omega$ cm)
fcc Cu	0.87	0.59	0.57	4.5	1.678
hcp Co	0.98	0.96	0.63	2.8	6.2
hcp Ru	0.74	1.30	0.65	2.1	7.8
bcc Mo	0.86	2.70	0.61	1.0	5.34

to ballistic transport property as follows:

$$\rho_0\lambda_0 = R_BA. \tag{18}$$

The product of ballistic resistance and cross-sectional area of the contact, donated by R_BA, corresponds to the Sharvin conductance [83]. This quantity is independent of scattering mechanisms but solely dependent on the electronic structure of the pure metal contacts. Equation (18) is known as a new perspective of Ohm's law, valid for diffusive transport regime as discussed in detail in the Ref. [82]. Our first-principles results of R_BA for different metals are presented in Table I for the same transport direction as films in Fig. 2. For example, the calculated R_BA of bulk Cu is 0.87×10^{-15} Ω m^2, which is in good agreement with previously reported values of conductance per spin 0.58×10^{15} Ω^{-1} m^{-2} [39,84], corresponding to an R_BA value of 0.86×10^{-15} Ω m^2.

Figure 5 plots the resistivity ρ_s versus the thickness d, and the fitting to Eq. (17) (in dashed lines) for the four different metals with $x = 0.5$ and $x = 0.1$ (in inset). For both high and low roughness concentrations in all metal films, ρ_s induced by surface roughness scattering increases rapidly as the thickness decreases, indicating a severe size effect. Among the four investigated metals, the resistivity size effect is the weakest in Cu thin films, while Mo thin films exhibit the strongest

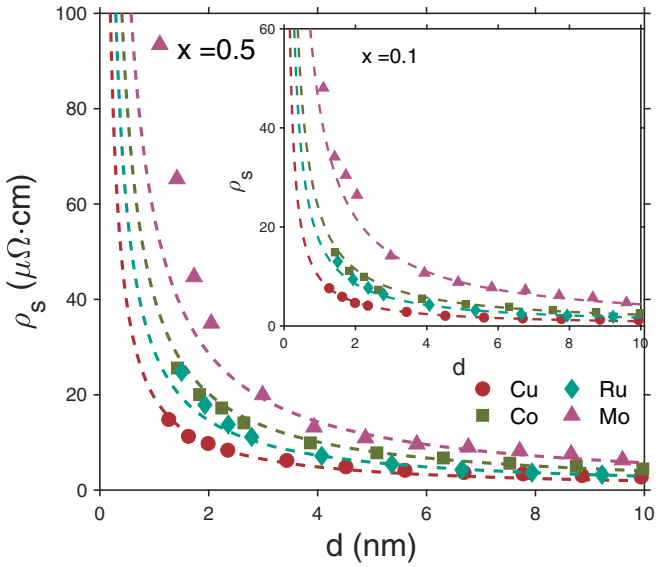

FIG. 5. Resistivity ρ_s vs thickness d for Cu, Co, Ru, and Mo thin film with roughness concentration $x = 0.5$ and $x = 0.1$ (inset). The dashed lines are fitting to Eq. (17).

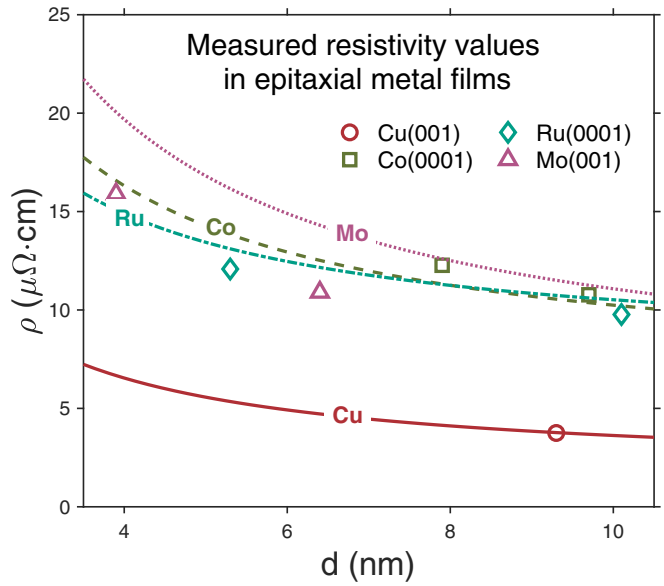

FIG. 6. Measured resistivity ρ vs thickness d of epitaxial metal layers. The data points are obtained from previous epitaxial metal layer experiments on Cu(001) [20], Co(0001) [15], Ru(0001) [13], and Mo(001) [85]. The dashed lines presents the total resistivity, which consist of the fitted result of surface scattering resistivity ρ_s for $x = 0.5$ and the bulk resistivity ρ_0 at room temperature (for the value of ρ_0, see Table I).

resistivity size effect. In particular, for the high concentration $x = 0.5$, the resistivity of Cu film increases from 2.75 to 14.82 μΩ cm as d decreases from 9.9 to 1.3 nm, while the resistivity of Mo increases from 6.29 μΩ cm at $d = 9.6$ nm to 93.43 μΩ cm at $d = 1.1$ nm, which is significantly higher than other metals. Moreover, the resistivity of Ru is slightly lower than the results of Co for both $x = 0.5$ and 0.1, presenting a similar size effect in ρ_s. We find that the present ρ_s for Cu agrees well with the previous first-principles studies [43,44], providing an important validation for our implementation. As shown in Fig. 5, the first-principles resistivity values for different thicknesses fit very well to Eq. (17) (with R_BA value calculated from first principles), indicating the $1/d$ dependence of resistivity for Cu, Co, Ru, and Mo thin film in the region of thickness below 10 nm, especially for Cu and Co. For Mo and Ru with $x = 0.5$, the $1/d$ dependence described by Eq. (17) presents an important underestimation from the first-principles calculations for $d < 2$ nm.

In recent experiments, the resistivity values of Cu, Co, Ru, and Mo ultrathin epitaxial metal films with thicknesses below 10 nm have been measured at room temperature [11,13,15,20,85]. Figure 6 presents a comparison between the experimental values and our first-principles resistivity results (by adding the bulk resistivity ρ_0 at room temperature (as listed in Table I). The dashed lines in Fig. 6 corresponds to the results for a roughness concentration of $x = 0.5$. The results depicted in Fig. 6 indicate that the first-principles prediction shows satisfactory consistency with the measured resistivity values of all four expitaxal metal films. Specifically, the predicted resistivity values for Cu, Co, and Ru are in good agreement with the experimental results, with deviations ranging from 0.5% to 8.5%. However, the experimental

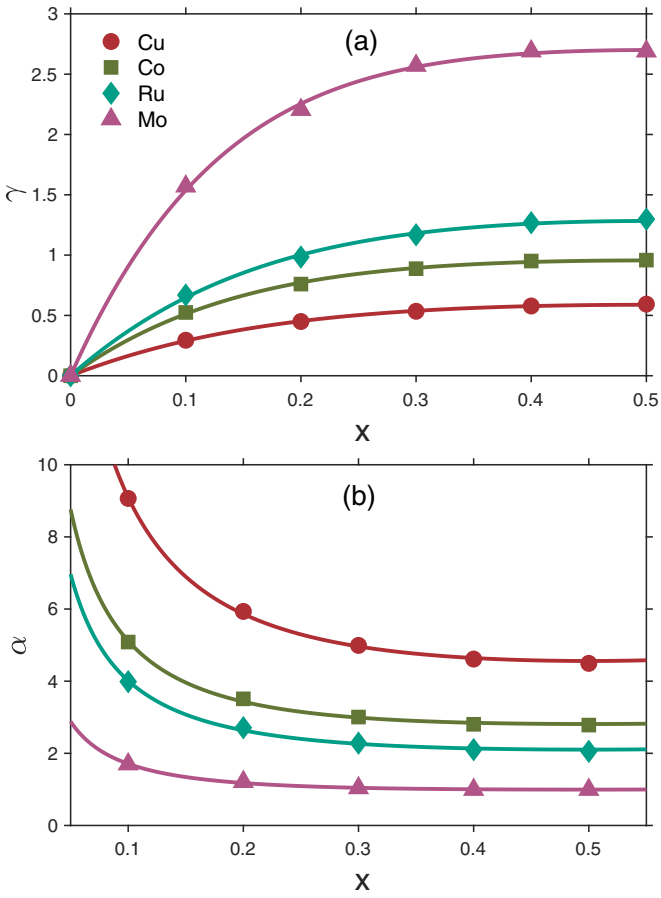

FIG. 7. (a) The intensity parameter of surface scatting γ_s vs roughness concentration x for Cu, Co, Ru, and Mo thin film. The solid lines represent the curve fitting to Eq. (19). (b) The proportionality constant α_s vs roughness concentration x for Cu, Co, Ru, and Mo thin film. The solid lines are from curve fitting.

resistivity values for Mo is about 30% lower than the corresponding the calculated results in dashed line. It should be noted that the first-principles results represents the up-limit of the theoretical results. The acceptable deviation between the simulation and experimental results can be attributed to differences between atomic-level surface roughness described by the disorder alloy model M_xVa_{1-x} with $x = 0.5$ and the realistic diffuse scattering surface observed in the experiment.

Figure 7(a) plots the fitting parameter γ_s versus surface roughness x to show the intensity of surface scattering by different x. Similarly to ρ_s as shown in Fig. 4, γ_s increases quickly at small x and becomes saturated as increasing x and reaches the maximal at $x = 0.5$. For a wide range of x ($x \geqslant 0.1$), the magnitude of γ_s for Mo is larger than 1.0 with a maximum of 2.69 and is significantly larger than other results, presenting the strongest intensity of surface scattering. Moreover, the surface roughness scattering in Mo is beyond the scope of the conventional FS model, as evidenced by the presence of a negative specular parameter p. Unlike the resistivity, γ_s value for Ru is higher than that of Co (for example, at $x = 0.5$, the γ_s values are 1.30 for Ru and 0.96 for Co). This can be attributed to the lower R_BA value of Ru, which is 0.74×10^{-15} Ω m^2, in constrst to that of Co(0.98×10^{-15} Ω m^2). The presence of $\gamma_s > 1.0$ in Mo and Ru indicates that the surface cannot be simply viewed as a boundary condition as in the FS model and surface roughness structure plays a key role in surface scattering. This has also been suggested by some experimental measurements [16] and other calculations [43]. Among all metals, Cu presents the smallest γ_s that is significantly lower than 1.0 with a maximum of 0.6, indicating the weakest effects of surface roughness scattering.

To go further, we find that, as shown in solid lines in Fig. 7 for all metals calculated, the γ_s results can be excellently fitted to the phenomenological model [37],

$$\frac{\gamma_s(x)}{\gamma_0} = 1 - x^{n\sigma} - (1-x)^{n\sigma}, \tag{19}$$

where γ_0 is the saturated value of surface scattering intensity at high concentrations, n is the density of surface sites, and σ is the scattering cross-sectional area of the metal atoms. In Ref. [37], Eq. (19) was first introduced to describe the x dependence of specular p in the FS model in Cu with O_2 adsorption. The normalized scattering intensity $\frac{\gamma_s(x)}{\gamma_0}$, ranges from 0.0 to 1.0 and represents the probability of an electron being scattered diffusively at surfaces. $x^{n\sigma} + (1-x)^{n\sigma}$ describes the probability of specular scattering at surfaces. The site density of Cu, Co, Ru, and Mo atoms in rough monolayers was calculated to be 10.85, 11.32, 9.94, and 10.10 nm^{-2}, respectively. By fitting the data, values of $n\sigma$ are obtained as follows: 6.18, 7.13, 6.46, and 6.16 for the respective Cu, Ru, Co, and Mo. Table I lists the obtained values of σ and the values of γ_0 that were used in the study for each metal. The obtained scattering cross-sectional area σ for the studied metals are were found to be similar, with values of 0.57, 0.63, 0.65, and 0.61 nm^2 for the respective Cu, Co, Ru, and Mo.

The mean-free path is a fundamental quantity for characterizing electron transport in the diffusive regime. By applying the new perspective of Ohm's law [82], we can write the following expression for the diffusive surface roughness scattering in the thin metal film,

$$\rho_s(d)\lambda_s(d) = R_BA, \tag{20}$$

where $\lambda_s(d)$ is effective mean free path of electron relaxation caused by surface scattering and is dependent on the film thickness. Here we neglect the small difference between bulk-derived ballistic R_B and film-derived R_B and use the bulk values for different metals. As a result, R_BA is considered a constant for a metal with a specific transport direction, and its dependence on the film thickness is neglected. Since the calculated resistivity results satisfy well the $1/d$ dependence, we can deduce that the value of λ_s is directly proportional to d, namely

$$\lambda_s(d) = \alpha_s \times d, \tag{21}$$

where the constant α_s characterizes the scattering intensity of surface roughness. Here we can find an important relationship for the quantities characterizing the surface roughness scattering, namely

$$\gamma_s\alpha_s = \tfrac{8}{3}. \tag{22}$$

Figure 7(b) presents the α_s as a function of x for Cu, Ru, Co, and Mo. The value of α_s decreases as the disorder

concentration x increases, due to the increase of surface scattering intensity. For all metals, the dependence of α_s on x is rather weak in the range $x > 0.2$, for example, α_s tended to be a constant with values of 4.5, 2.8, 2.1, and 1.0 for Cu, Ru, Co, and Mo, respectively. The dependence of α_s on x is most significant at low concentrations. For example, in the studied range of $0.1 \leqslant x \leqslant 0.5$, the Cu thin film exhibits the largest α_s value, which decreases from 9.0 to 4.5, indicating the weakest strength of surface roughness scattering compared to the other metals. On the other hand, the α_s value for Mo films has the smallest magnitude and the weakest dependence on x, changing from 2.1 at $x = 0.1$ to 1.0 at $x = 0.5$. By applying the Eqs. (19) and (22), it is found that the calculated α_s values can be very well fitted to the relation $\frac{\alpha_0}{\alpha_s(x)} = 1 - x^{n\sigma} - (1-x)^{n\sigma}$ with α_0 values of 4.5, 2.8, 2.1, and 1.0 for the respective Cu, Co, Ru, and Mo films. Table I summarizes the parameters obtained in this study, which can be used to predict the size effect of metal resistivity and identify potential replacement metals.

IV. CONCLUSION

In summary, we used first-principles quantum transport simulations combined with the nonequilibrium mean-field theory to investigate the resistivity size effect of surface roughness scattering in Cu, Co, Ru, and Mo thin films with different thickness d and roughness concentration x. We calculated the film resistance as a function of scattering region length l and obtained the resistivity ρ_s. Our results showed that the resistivity increases rapidly as the thickness decreases with a $1/d$ dependence. For the same thickness d, Mo thin films exhibit significantly higher ρ_s than other metals, Co presents a ρ_s value 1.6 times that of Cu, while Ru's ρ_s is slightly higher than Cu values. Moreover, we obtain the γ_s versus the roughness concentration x to characterize the intensity of surface roughness scattering. we find that γ_s can be very well described by the relation $\frac{\gamma_s}{\gamma_0} = 1 - x^{n\sigma} - (1-x)^{n\sigma}$. By applying the relation $\rho_s \lambda_s = R_B A$, we obtain the values of α_s versus x in the mean-free path $\lambda_s = \alpha_s \times d$ for surface roughness scattering. It is found that, at high roughness concentration with $x > 0.2$, α_s tended to be a constant with values of 4.5, 2.8, 2.1, and 1.0 for Cu, Ru, Co, and Mo, respectively. The resistivity results are in good agreement with the experimental measurements of the epitaxial metal layer, and the fitting parameters are consistent with previous literature reports. We conclude that Ru has shown competitiveness in the resistivity size effect of surface roughness compared to Mo and Co and could serve as an alternative to Cu interconnect for future technology nodes.

ACKNOWLEDGMENTS

Y.K. acknowledges financial support from NSFC (Grants No. 12227901 and No. 11874265). The authors thank the HPC platform of ShanghaiTech University for providing the computational facility.

[1] H. D. Liu, Y. P. Zhao, G. Ramanath, S. P. Murarka, and G. C. Wang, Thickness dependent electrical resistivity of ultrathin (<40 nm) Cu films, Thin Solid Films **384**, 151 (2001).

[2] S. M. Rossnagel and T. S. Kuan, Alteration of Cu conductivity in the size effect regime, J. Vac. Sci. Technol. B **22**, 240 (2004).

[3] J. J. Plombon, E. Andideh, V. M. Dubin, and J. Maiz, Influence of phonon, geometry, impurity, and grain size on copper line resistivity, Appl. Phys. Lett. **89**, 113124 (2006).

[4] D. Josell, S. H. Brongersma, and Z. Tőkei, Size-dependent resistivity in nanoscale interconnects, Annu. Rev. Mater. Res. **39**, 231 (2009).

[5] R. L. Graham, G. B. Alers, T. Mountsier, N. Shamma, S. Dhuey, S. Cabrini, R. H. Geiss, D. T. Read, and S. Peddeti, Resistivity dominated by surface scattering in sub-50 nm Cu wires, Appl. Phys. Lett. **96**, 042116 (2010).

[6] J. S. Chawla, F. Gstrein, K. P. O'Brien, J. S. Clarke, and D. Gall, Electron scattering at surfaces and grain boundaries in Cu thin films and wires, Phys. Rev. B **84**, 235423 (2011).

[7] C. Pan and A. Naeemi, A proposal for a novel hybrid interconnect technology for the end of roadmap, IEEE Electr. Device Lett. **35**, 250 (2014).

[8] J. M. Roberts, A. P. Kaushik, and J. S. Clarke, Resistivity of sub-30 nm copper lines, in *IEEE International Interconnect Technology Conference and IEEE Materials for Advanced Metallization Conference (IITC/MAM)* (IEEE, Los Alamitos, CA, 2015), pp. 341–344.

[9] International Roadmap for Devices and Systems (2022).

[10] E. V. Barnat, D. Nagakura, P.-I. Wang, and T.-M. Lu, Real time resistivity measurements during sputter deposition of ultrathin copper films, J. Appl. Phys. **91**, 1667 (2002).

[11] J. M. Purswani and D. Gall, Electron scattering at single crystal Cu surfaces, Thin Solid Films **516**, 465 (2007).

[12] K. Barmak and K. R. Coffey, Epitaxial metals for interconnects beyond Cu: Resistivity, reliability, in *International Symposium on VLSI Technology, Systems and Applications (VLSI-TSA)* (2020), pp. 115–116.

[13] E. Milosevic, S. Kerdsongpanya, A. Zangiabadi, K. Barmak, K. R. Coffey, and D. Gall, Resistivity size effect in epitaxial Ru (0001) layers, J. Appl. Phys. **124**, 165105 (2018).

[14] E. Milosevic, S. Kerdsongpanya, and D. Gall, The resistivity size effect in epitaxial Ru(0001) and Co(0001) layers, in *IEEE Nanotechnology Symposium (ANTS)* (IEEE, Los Alamitos, CA, 2018), pp. 1–5.

[15] E. Milosevic, S. Kerdsongpanya, M. E. McGahay, A. Zangiabadi, K. Barmak, and D. Gall, Resistivity scaling and electron surface scattering in epitaxial Co(0001) layers, J. Appl. Phys. **125**, 245105 (2019).

[16] P. Y. Zheng, T. Zhou, B. J. Engler, J. S. Chawla, R. Hull, and D. Gall, Surface roughness dependence of the electrical resistivity of W(001) layers, J. Appl. Phys. **122**, 095304 (2017).

[17] D. Gall, The search for the most conductive metal for narrow interconnect lines, J. Appl. Phys. **127**, 050901 (2020).

[18] K. Fuchs, The conductivity of thin metallic films according to the electron theory of metals, Math. Proc. Cambr. Philos. Soc. **34**, 100 (1938).

[19] E. H. Sondheimer, The mean free path of electrons in metals, Adv. Phys. **50**, 499 (2001).

[20] P. Y. Zheng, R. P. Deng, and D. Gall, Ni doping on Cu surfaces: Reduced copper resistivity, Appl. Phys. Lett. **105**, 131603 (2014).

[21] P. Zheng, T. Zhou, and D. Gall, Electron channeling in TiO_2 coated Cu layers, Semicond. Sci. Technol. **31**, 055005 (2016).

[22] D. Choi, X. Liu, P. K. Schelling, K. R. Coffey, and K. Barmak, Failure of semiclassical models to describe resistivity of nanometric, polycrystalline tungsten films, J. Appl. Phys. **115**, 104308 (2014).

[23] Y. P. Timalsina, X. Shen, G. Boruchowitz, Z. Fu, G. Qian, M. Yamaguchi, G.-C. Wang, K. M. Lewis, and T.-M. Lu, Evidence of enhanced electron-phonon coupling in ultrathin epitaxial copper films, Appl. Phys. Lett. **103**, 191602 (2013).

[24] J. S. Chawla and D. Gall, Specular electron scattering at single-crystal Cu(001) surfaces, Appl. Phys. Lett. **94**, 252101 (2009).

[25] J. S. Chawla, X. Y. Zhang, and D. Gall, Epitaxial TiN(001) wetting layer for growth of thin single-crystal Cu(001), J. Appl. Phys. **110**, 043714 (2011).

[26] J. S. Chawla and D. Gall, Epitaxial Ag(001) grown on MgO(001) and TiN(001): Twinning, surface morphology, and electron surface scattering, J. Appl. Phys. **111**, 043708 (2012).

[27] J. S. Chawla, X. Y. Zhang, and D. Gall, Effective electron mean free path in TiN(001), J. Appl. Phys. **113**, 063704 (2013).

[28] R. E. Prange and T.-W. Nee, Quantum spectroscopy of the low-field oscillations in the surface impedance, Phys. Rev. **168**, 779 (1968).

[29] Y. Namba, Resistivity and temperature coefficient of thin metal films with rough surface, Jpn. J. Appl. Phys. **9**, 1326 (1970).

[30] Z. Tešanović, M. V. Jarić, and S. Maekawa, Quantum Transport and Surface Scattering, Phys. Rev. Lett. **57**, 2760 (1986).

[31] D. Calecki, Galvanomagnetic phenomena and surface roughness in thin metallic films, Phys. Rev. B **42**, 6906 (1990).

[32] L. Sheng, D. Y. Xing, and Z. D. Wang, Transport theory in metallic films: Crossover from the classical to the quantum regime, Phys. Rev. B **51**, 7325 (1995).

[33] R. C. Munoz, G. Vidal, G. Kremer, L. Moraga, and C. Arenas, Surface-induced resistivity of gold films on mica: comparison between the classical and the quantum theory, J. Phys.: Condens. Matter **11**, L299 (1999).

[34] P. Zheng and D. Gall, The anisotropic size effect of the electrical resistivity of metal thin films: Tungsten, J. Appl. Phys. **122**, 135301 (2017).

[35] D. Choi, M. Moneck, X. Liu, S. J. Oh, C. R. Kagan, K. R. Coffey, and K. Barmak, Crystallographic anisotropy of the resistivity size effect in single crystal tungsten nanowires, Sci. Rep. **3**, 2591 (2013).

[36] J. M. Rickman and K. Barmak, Simulation of electrical conduction in thin polycrystalline metallic films: Impact of microstructure, J. Appl. Phys. **114**, 133703 (2013).

[37] J. S. Chawla, F. Zahid, H. Guo, and D. Gall, Effect of O_2 adsorption on electron scattering at Cu(001) surfaces, Appl. Phys. Lett. **97**, 132106 (2010).

[38] F. Zahid, Y. Ke, D. Gall, and H. Guo, Resistivity of thin Cu films coated with Ta, Ti, Ru, Al, and Pd barrier layers from first principles, Phys. Rev. B **81**, 045406 (2010).

[39] V. Timoshevskii, Y. Ke, H. Guo, and D. Gall, The influence of surface roughness on electrical conductance of thin Cu films: An ab initio study, J. Appl. Phys. **103**, 113705 (2008).

[40] Y.-N. Zhao, S.-X. Qu, and K. Xia, Influence of the surface structure and vibration mode on the resistivity of Cu films, J. Appl. Phys. **110**, 064312 (2011).

[41] T. Zhou, P. Zheng, S. C. Pandey, R. Sundararaman, and D. Gall, The electrical resistivity of rough thin films: A model based on electron reflection at discrete step edges, J. Appl. Phys. **123**, 155107 (2018).

[42] A. Sanchez-Soares, S. L. T. Jones, J. J. Plombon, A. P. Kaushik, R. E. Nagle, J. S. Clarke, and J. C. Greer, Effect of strain, thickness, and local surface environment on electron transport properties of oxygen-terminated copper thin films, Phys. Rev. B **94**, 155404 (2016).

[43] T. Zhou and D. Gall, Resistivity scaling due to electron surface scattering in thin metal layers, Phys. Rev. B **97**, 165406 (2018).

[44] Y. Ke, F. Zahid, V. Timoshevskii, K. Xia, D. Gall, and H. Guo, Resistivity of thin Cu films with surface roughness, Phys. Rev. B **79**, 155406 (2009).

[45] Y. Ke, K. Xia, and H. Guo, Disorder Scattering in Magnetic Tunnel Junctions: Theory of Nonequilibrium Vertex Correction, Phys. Rev. Lett. **100**, 166805 (2008).

[46] J. Yan and Y. Ke, Generalized nonequilibrium vertex correction method in coherent medium theory for quantum transport simulation of disordered nanoelectronics, Phys. Rev. B **94**, 045424 (2016).

[47] Y. Zhang, J. Zhai, Z. Chen, Q. Zhang, and Y. Ke, First-principles nonequilibrium dynamical cluster theory for quantum transport simulations of disordered nanoelectronic devices, Phys. Rev. B **104**, 115412 (2021).

[48] Y. Zhang, Q. Zhang, Y. Ke, and K. Xia, Giant influence of clustering and anti-clustering of disordered surface roughness on electronic tunneling, Chin. Phys. Lett. **39**, 087301 (2022).

[49] D. Gall, Metals for low-resistivity interconnects, in *IEEE International Interconnect Technology Conference (IITC)* (IEEE, Los Alamitos, CA, 2018), pp. 157–159.

[50] C. Adelmann, K. Sankaran, S. Dutta, A. Gupta, S. Kundu, G. Jamieson, K. Moors, N. Pinna, I. Ciofi, S. V. Eishocht *et al.*, Alternative metals: From ab initio screening to calibrated narrow line models, in *IEEE International Interconnect Technology Conference (IITC)* (IEEE, Los Alamitos, CA, 2018), pp. 154–156.

[51] D. Gall, Electron mean free path in elemental metals, J. Appl. Phys. **119**, 085101 (2016).

[52] C. Adelmann, L. G. Wen, A. P. Peter, Y. K. Siew, K. Croes, J. Swerts, M. Popovici, K. Sankaran, G. Pourtois, S. V. Elshocht *et al.*, Alternative metals for advanced interconnects, in *IEEE International Interconnect Technology Conference (IITC)* (IEEE, Los Alamitos, CA, 2014), pp. 173–176.

[53] S. Dutta, S. Kundu, L. Wen, G. Jamieson, K. Croes, A. Gupta, J. Bömmels, C. J. Wilson, C. Adelmann, and Z. Tokei, Ruthenium interconnects with 58 nm2 cross-section area using a metal-spacer process, in *IEEE International Interconnect Technology Conference (IITC)* (IEEE, Los Alamitos, CA, 2017), pp. 1–3.

[54] L. G. Wen, P. Roussel, O. V. Pedreira, B. Briggs, B. Groven, S. Dutta, M. I. Popovici, N. Heylen, I. Ciofi, K. Vanstreels *et al.*, Atomic layer deposition of ruthenium with TiN interface for sub-10 nm advanced interconnects beyond copper, ACS Appl. Mater. Interf. **8**, 26119 (2016).

[55] L. G. Wen, C. Adelmann, O. V. Pedreira, S. Dutta, M. Popovici, B. Briggs, N. Heylen, K. Vanstreels, C. J. Wilson, S. V. Elshocht *et al.*, Ruthenium metallization for advanced

interconnects, in *IEEE International Interconnect Technology Conference/Advanced Metallization Conference (IITC/AMC)* (IEEE, Los Alamitos, CA, 2016), pp. 34–36.

[56] V. Kamineni, M. Raymond, S. Siddiqui, F. Mont, S. Tsai, C. Niu, A. Labonte, C. Labelle, S. Fan, B. Peethala *et al.*, Tungsten and cobalt metallization: A material study for mol local interconnects, in *IEEE International Interconnect Technology Conference/Advanced Metallization Conference (IITC/AMC)* (IEEE, Los Alamitos, CA, 2016), pp. 105–107.

[57] T. Nogami, R. Patlolla, J. Kelly, B. Briggs, H. Huang, J. Demarest, J. Li, R. Hengstebeck, X. Zhang, G. Lian *et al.*, Cobalt/copper composite interconnects for line resistance reduction in both fine and wide lines, in *IEEE International Interconnect Technology Conference (IITC)* (IEEE, Los Alamitos, CA, 2017), pp. 1–3.

[58] F. Griggio, J. Palmer, F. Pan, N. Toledo, A. Schmitz, I. Tsameret, R. Kasim, G. Leatherman, J. Hicks, A. Madhavan *et al.*, Reliability of dual-damascene local interconnects featuring cobalt on 10 nm logic technology, in *IEEE International Reliability Physics Symposium (IRPS)* (IEEE, Los Alamitos, CA, 2018), p. 6E–3.

[59] C. Auth, A. Aliyarukunju, M. Asoro, D. Bergstrom, V. Bhagwat, J. Birdsall, N. Bisnik, M. Buehler, V. Chikarmane, G. Ding *et al.*, A 10 nm high performance and low-power CMOS technology featuring 3 rd generation finfet transistors, self-aligned quad patterning, contact over active gate and cobalt local interconnects, in *IEEE International Electron Devices Meeting (IEDM)* (IEEE, Los Alamitos, CA, 2017), p. 29-1.

[60] V. Founta, J.-P. Soulié, K. Sankaran, K. Vanstreels, K. Opsomer, P. Morin, P. Lagrain, A. Franquet, D. Vanhaeren, T. Conard *et al.*, Properties of ultrathin molybdenum films for interconnect applications, Materialia **24**, 101511 (2022).

[61] Q. Zhang, J. Yan, Y. Zhang, and Y. Ke, Exact muffin tin orbital based first-principles method for electronic-structure and electron-transport simulation of device materials, Phys. Rev. B **100**, 075134 (2019).

[62] Z. Chen, Q. Zhang, Y. Zhang, L. Wang, M. Sang, and Y. Ke, Exact muffin-tin orbital based fully relativistic simulation of device materials: Electronic charge and spin current, Phys. Rev. B **102**, 035405 (2020).

[63] O. Krogh, Andersen, V. Kumar, and A. Mookerjee, *Lectures on Methods of Electronic Structure Calculations* (World Scientific, Singapore, 1995).

[64] O. K. Andersen, C. Arcangeli, R. W. Tank, T. Saha-Dasgupta, G. Krier, O. Jepsen, and I. Dasgupta, Third-generation TB-LMTO, MRS Proc. **491**, 3 (1997).

[65] O. K. Andersen and T. Saha-Dasgupta, Muffin-tin orbitals of arbitrary order, Phys. Rev. B **62**, R16219 (2000).

[66] L. Vitos, Total-energy method based on the exact muffin-tin orbitals theory, Phys. Rev. B **64**, 014107 (2001).

[67] L. Vitos, *Computational Quantum Mechanics for Materials Engineers: The EMTO Method and Applications* (Springer Science & Business Media, New York, 2007).

[68] O. K. Andersen, T. Saha-Dasgupta, R. W. Tank, C. Arcangeli, O. Jepsen, and G. Krier, *Electronic Structure and Physical Properties of Solids* (Springer, Berlin, 2000).

[69] L. V. Keldysh *et al.*, Diagram technique for nonequilibrium processes, Sov. Phys. JETP **20**, 1018 (1965).

[70] L. Vitos, H. L. Skriver, B. Johansson, and J. Kollár, Application of the exact muffin-tin orbitals theory: The spherical cell approximation, Comput. Mater. Sci. **18**, 24 (2000).

[71] I. Turek, V. Drchal, J. Kudrnovsky, M. Sob, and P. Weinberger, *Electronic Structure of Disordered Alloys, Surfaces and Interfaces* (Springer Science & Business Media, Berlin, 1997).

[72] Q. Wei, J. Zhai, Z. Ning, and Y. Ke, Mean-field approach for anderson-type off-diagonal disorder, Phys. Rev. B **106**, 214205 (2022).

[73] Z. Cheng, J. Zhai, Q. Zhang, and Y. Ke, Auxiliary coherent medium theory for lattice vibrations in random binary alloys with mass and force-constant disorders, Phys. Rev. B **99**, 134202 (2019).

[74] Z. Cheng, M. Sang, J. Zhai, and Y. Ke, Phonon dispersion of binary alloys with auxiliary coherent potential approximation, Phys. Rev. B **100**, 214206 (2019).

[75] J. Zhai, R. Xue, Z. Cheng, and Y. Ke, Direct comparison of auxiliary and itinerant coherent potential approximations for disordered lattice vibration: Phonon spectral and transport properties, Phys. Rev. B **104**, 024205 (2021).

[76] J. Zhai, Q. Zhang, Z. Cheng, J. Ren, Y. Ke, and B. Li, Anomalous transparency induced by cooperative disorders in phonon transport, Phys. Rev. B **99**, 195429 (2019).

[77] G. Bruzzone, The binary systems calcium-copper, strontium-copper and barium-copper, J. Less-Common Met. **25**, 361 (1971).

[78] T. Pan, G. W. D. Spratt, L. Tang, and D. E. Laughlin, Magnetic properties and microstructure of evaporated Co oxide tape media, J. Magn. Magn. Mater. **155**, 309 (1996).

[79] I. G. Puzachenko, Thermostatical foundations of geography, Izv. Ross. Akad. Nauk. Seriya Geogr. **0**, 21 (2016).

[80] A. Taylor and N. J. Doyle, The constitution diagram of the tungsten-molybdenum-osmium system, J. Less-Common Met. **9**, 190 (1965).

[81] S. H. Vosko, L. Wilk, and M. Nusair, Accurate spin-dependent electron liquid correlation energies for local spin density calculations: A critical analysis, Can. J. Phys. **58**, 1200 (1980).

[82] S. Datta, *Lessons from Nanoelectronics: A New Perspective on Transport* (World Scientific, Singapore, 2018).

[83] Y. V. Sharvin, On the possible method for studying fermi surfaces, Zh. Eksp. Teor. Fiz. 48 (1965).

[84] K. M. Schep, P. J. Kelly, and G. E. W. Bauer, Ballistic transport and electronic structure, Phys. Rev. B **57**, 8907 (1998).

[85] A. Jog, P. Zheng, T. Zhou, and D. Gall, Anisotropic resistivity size effect in epitaxial Mo(001) and Mo(011) layers, Nanomaterials **13**, 957 (2023).